

1 **Simulating the Holocene deglaciation across a marine terminating portion of southwestern**
2 **Greenland in response to marine and atmospheric forcings**

3
4 Joshua K. Cuzzone¹, Nicolás E. Young², Mathieu Morlighem³, Jason P. Briner⁴, Nicole-Jeanne
5 Schlegel⁵

6
7 1University of California Los Angeles, Los Angeles, CA, USA
8 2Lamont-Doherty Earth Observatory, Columbia University, New York, NY, USA
9 3Department of Earth Sciences, Dartmouth College, Hanover, NH, USA.
10 4Department of Geology, University at Buffalo, Buffalo, NY, USA
11 5NASA Jet Propulsion Laboratory, California Institute of Technology, Pasadena, CA, USA.

12
13 *Correspondence to:* Joshua K. Cuzzone (Joshua.K.Cuzzone@jpl.nasa.gov)

14 **Abstract**

15
16 Numerical simulations of the Greenland Ice Sheet (GrIS) over geologic timescales can greatly
17 improve our knowledge of the critical factors driving GrIS demise during climatically warm
18 periods, which has clear relevance for better predicting GrIS behavior over the upcoming
19 centuries. To assess the fidelity of these modeling efforts, however, observational constraints of
20 past ice-sheet change are needed. Across southwestern Greenland, geologic records detail
21 Holocene ice retreat across both terrestrial-based and marine terminating environments, providing
22 an ideal opportunity to rigorously benchmark model simulations against geologic reconstructions
23 of ice-sheet change. Here, we present regional ice sheet modeling results using the Ice-sheet and
24 Sea-level System Model (ISSM) of Holocene ice sheet history across an extensive fjord region in
25 southwestern Greenland covering the landscape around the Kangiata Nunaata Sermia (KNS)
26 glacier and extending outward along the 200 km **Nuup Kangerula (Godthåbsfjord)**. Our
27 simulations, forced by reconstructions of Holocene climate and recently implemented calving
28 laws, assess the sensitivity of ice retreat across the KNS region to atmospheric and oceanic
29 forcing. Our simulations reveal that the geologically reconstructed ice retreat across the **terrestrial**
30 **landscape in the study area was likely driven by fluctuations in surface mass balance in response**
31 **to Early Holocene warming – and likely not influenced significantly by the response of adjacent**
32 **outlet glaciers to calving and ocean-induced melting. The impact of ice calving within fjords,**
33 **however, plays a significant role by enhancing ice discharge at the terminus, leading to interior**
34 **thinning up to the ice divide that is consistent with reconstructed magnitudes of Early Holocene**
35 **ice thinning. Our results, benchmarked against geologic constraints of past ice margin change,**
36 **suggest that while calving did not strongly influence Holocene ice margin migration across**
37 **terrestrial portions of the KNS forefield, it strongly impacted regional mass loss. While these**
38 **results imply that the implementation and resolution of ice calving in paleo ice flow models is**
39 **important towards making more robust estimations of past ice mass change, they also illustrate the**
40 **importance these processes have on contemporary and future long term ice mass change across**
41 **similar fjord-dominated regions of the GrIS.**

42
43 **1. Introduction**
44

Deleted: novel

Deleted: bedrock

Deleted: above sea-level

Deleted: early Holocene

Deleted: early Holocene

Deleted: may provide an analog to how similar fjord-dominated regions of the GrIS may respond to future warming, they also

Deleted: illustrate

Deleted: ling

55 Over the past few decades, the Greenland Ice Sheet (GrIS) has experienced accelerating ice mass
56 loss driven by increases in surface melt, runoff, and dynamic ice loss at marine terminating margins
57 (IMBIE, 2019). While projected mass loss from the GrIS is expected to be driven increasingly by
58 its surface mass balance (SMB; Enderlin et al., 2014; Vizcaino et al., 2015; Goelzer et al., 2020)
59 and attendant meltwater runoff (Fettweis et al., 2008; Lenaerts et al., 2018), considerable
60 uncertainty exists regarding how oceanic forcing will influence GrIS mass loss, particularly
61 through ice calving processes (Goelzer et al., 2020; Choi et al., 2021). The satellite-based
62 observational record of GrIS change only spans a few decades making it difficult to identify and
63 disentangle the key drivers of GrIS mass change, and to understand over which timescales they
64 operate. Fortunately, geologic records detailing the retreat history of the GrIS provide an
65 important metric for evaluating numerical ice sheet models and help pinpoint the contributions of
66 various driving mechanisms to GrIS change. When combined, numerical ice sheet models and
67 geologic reconstructions can provide key insights into GrIS behavior in a warming climate across
68 centennial to millennial timescales.

Deleted: smb

70 The current interglacial, the Holocene (the last 11.7 ka), is characterized by prolonged warmth
71 with proxy records suggesting that temperatures during the early to Middle Holocene were 3 ± 1 °C
72 warmer than the pre-industrial period (Briner et al., 2016; Lecavalier et al., 2017), which drove
73 widespread retreat of the GrIS margin at a rate of ice mass loss exceeding 20th century values
74 (1900-2000 CE Young and Briner, 2015; Briner et al., 2020). Across southwestern Greenland, a
75 detailed geologic record of Holocene ice-margin retreat encompassing both terrestrial and marine
76 terminating environments exists, providing an ideal testbed for ice sheet models to test the
77 sensitivity of past ice margin migration to atmospheric and marine forcings (Larsen et al., 2014;
78 Lesnek et al., 2020; Young et al., 2020; Young et al., 2021). Where land-based ice existed, well-
79 dated moraine sequences constrain ~120 km of ice retreat from the present-day coastline to just
80 outboard of the present-day ice margin (Lesnek et al., 2020; Young et al., 2020), and have been
81 shown by ice sheet models to be driven by negative SMB in response to Early Holocene warming
82 (Cuzzone et al., 2019; Downs et al., 2020; Briner et al., 2020).

Deleted: ciation

Deleted: middle Holocene

Deleted: S

Deleted: smb

Deleted: early Holocene

84 Unlike the land-based portions of Southwest Greenland however, across the marine based region
85 covering the forefield around Kangiata Nunaata Sermia (KNS; Figure 1), it remains unknown what
86 drove this rapid ice margin retreat during the Early Holocene (Young et al., 2021). While links
87 between atmospheric warming and runoff induced terminus retreat have been implicated as
88 reasons for the most recent historical retreat across the KNS region (Lea et al., 2014a,b), the longer
89 term triggers of rapid Holocene ice retreat are not constrained by the geologic data alone. Because
90 of the well dated chronology detailing Holocene ice retreat across this region however, ice sheet
91 models are well poised to address questions surrounding the scales of influence atmospheric and
92 oceanic forcings play on long term ice margin and mass change. However, as many paleo ice flow
93 models employ model grids that are relatively coarse (10 km or greater), ice margin migration and
94 ultimately ice discharge through fjord systems may be poorly simulated or not captured as many
95 models cannot resolve the complex and narrow fjord geometries found across the GrIS (Cuzzone
96 et al., 2019).

Deleted: early Holocene

97
98 Building on recent advances in calving front dynamics in the Ice Sheet and Sea-level System
99 Model (ISSM; Larour et al., 2012), we use a high-resolution regional ice sheet model to investigate
100 the Holocene ice retreat across the KNS forefield. Our simulations build on prior ice modeling

108 efforts across southwestern Greenland that were driven by novel reconstructions of past climate
109 (Badgley et al., 2020; Briner et al., 2020). Where our past ice flow modeling efforts excluded ice
110 ocean-interactions (Briner et al., 2020), our simulations presented here take advantage of recent
111 implementation of physically based calving schemes in ISSM to specifically address how
112 Holocene ice retreat across the KNS forefield was influenced by marine and atmospheric forcing's.
113 Moreover, this work provides a foundation for future experiments using ISSM to simulate the
114 influence of ice-ocean interactions on the Holocene variability of the broader GrIS.
115

Deleted: S

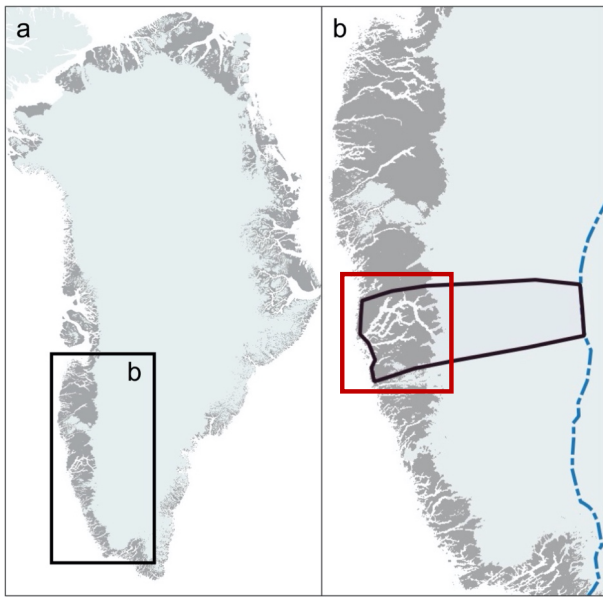


Figure 1. a.) The Greenland Ice Sheet. Highlighted is southwestern Greenland, where the ice model domain resides. b.) Southwestern Greenland. The ice model domain is outlined (bold black line), extending between the present-day coastline and ice divide (dashed blue line; Rignot and Mouginot, 2012). The red box corresponds to the area in figures 5, 6 and 8.

116
117 **2. Holocene Ice Retreat across the KNS Forefield**
118

119 Decades of radiocarbon dating and, more recently, cosmogenic ¹⁰Be dating, track the retreat of the
120 GrIS in the KNS region through the Holocene (Weidick et al., 2012 and references therein; Larsen
121 et al., 2014; Young et al., 2021). Minimum-limiting radiocarbon ages from the outer coast near
122 Nuuk range from ca. 11.2 to 10.6 ka BP., which is mimicked by ¹⁰Be ages of ca. 10.7 and 10.4 ka
123 BP (Figure 2). Between the outer coast and the modern GrIS margin at KNS are numerous
124 radiocarbon and ¹⁰Be ages that are largely indistinguishable and require rapid deglaciation of the
125 region spanning about a millennium (Weidick et al., 2012; Larsen et al., 2014; Young et al., 2021).
126 Perhaps most relevant here are ¹⁰Be ages in the immediate KNS region from just beyond the
127 historical ice limit that suggest KNS had retreated within or near its current position by ca. 10.3 ka

129 (Young et al., 2021). Radiocarbon ages from raised marine deposits, which require ice-free
 130 conditions, adjacent to the main KNS fjord appear slightly younger than regional ^{10}Be ages. These
 131 radiocarbon ages, however, are minimum-limiting ages and an upfjord radiocarbon age of ca. 10.2
 132 ka from a bivalve reworked by a KNS readvance requires that the main fjord deglaciated prior to
 133 ca. 10.2 ka (Figure 2). Collectively, the radiocarbon and ^{10}Be ages suggest rapid and synchronous
 134 deglaciation of both the landscape and fjord systems between the outer coast near Nuuk and the
 135 modern margin at KNS. Lastly, ^{10}Be ages from slightly beyond the historical limit to the north and
 136 south of KNS are slightly younger suggesting that these ice margins may have lagged behind ice
 137 retreat in the immediate KNS region (Figure 2).
 138

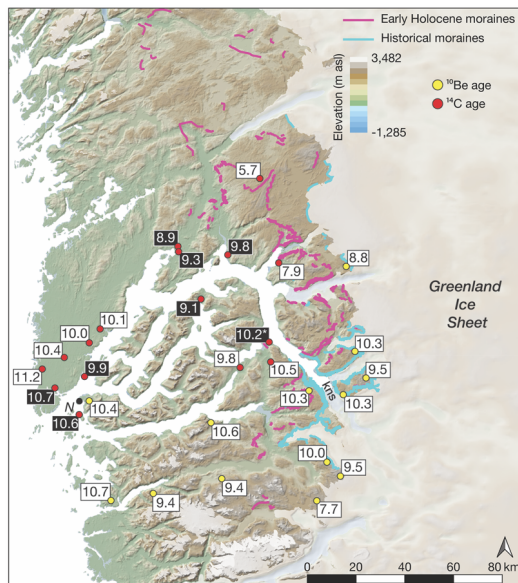


Figure 2. KNS region with geological constraints that track GrIS retreat in the Early Holocene. Radiocarbon ages (red circles) and ^{10}Be ages (yellow circles) are from Weidick et al. (2012), Larsen et al. (2014), and Young et al. (2021). For figure clarity, we only show the mean deglaciation age at each site (see Young et al., 2021 for full site descriptions). Radiocarbon and ^{10}Be across the immediate KNS region are similar and reveal that deglaciation of the coast occurred ca. 11.2-10.7 ka and KNS had retreated near or within its modern extent by ca. 10.3 ka. Radiocarbon ages in white text and black background are from marine deposits and constrain the timing of retreat within the main fjord. Figure has been modified from Young et al. (2021).

Deleted: early Holocene

139
 140 **3. Model description and setup**
 141
 142 **3.1 Ice Sheet Model**
 143

144 We rely on ISSM, a thermomechanical finite-element ice sheet model, to simulate the Holocene
 145 ice history across the KNS forefield, and follow similar published model setups (Cuzzone et al.,
 146 2019; Briner et al., 2020). The higher-order approximation of Blatter (1995) and Pattyn (2003) is
 147 used to solve the momentum balance equations. Our model domain centers on the KNS and
 148 Godthåbsfjord forefield, extending from the present-day coastline, where geologic observations
 149 show ice resided at the end of the Younger Dryas (Larsen et al., 2014; Lesnek et al., 2020) to the
 150 present-day ice divide (Figure 1b; Rignot and Mouginot, 2012). The northern and southern
 151 boundaries of our model domain are chosen to represent regions of minimal north-south across
 152 boundary flow based on Holocene ice sheet simulations of southwestern Greenland (Briner et al.,
 153 2020). Anisotropic mesh adaptation is used to create a non-uniform model mesh that varies based
 154 upon gradients in bedrock topography from BedMachine v3 (Morlighem et al., 2017). Because
 155 fjord width across our domain is often <5 km and high-resolution grids are necessary for capturing
 156 grounding line dynamics (1 km; Seroussi and Morlighem, 2018), the horizontal mesh resolution
 157 varies from 1 km in fjords and areas of high bedrock relief to 15 km where the bedrock relief is
 158 low (Figure 3).

159
 160 To capture the thermal evolution of the ice, our model uses an enthalpy formulation (Aschwanden
 161 et al., 2012) that captures both temperate and cold ice. We impose transient air temperatures at
 162 the surface and a constant but spatially varying geothermal heat flux at the base (Shapiro and
 163 Ritzwoller, 2004) and our model contains only five vertical layers in order to reduce computational
 164 load (Cuzzone et al., 2018; Cuzzone et al., 2019). In order to capture sharp thermal gradients near
 165 the base and simulate the vertical distribution of temperature within the ice, we use quadratic finite
 166 elements (P1xP2) along the z-axis for the vertical interpolation following Cuzzone et al. (2018).
 167 This methodology has been successfully applied to simulate the transient behavior of the GrIS
 168 across geologic timescales and the contemporary period (Cuzzone et al., 2019; Briner et al., 2020;
 169 Smith-Johnson et al., 2020).

170
 171 We use a linear friction law and, similar to Briner et al. (2020), we construct a spatially varying
 172 basal friction coefficient (k) under areas covered by the present-day ice sheet using inverse
 173 methods (Morlighem et al., 2010; Larour et al., 2012) that satisfies the best match between
 174 modeled and satellite-derived surface velocities (Rignot and Mouginot, 2012):

$$175 \quad \tau_b = -k^2 N v_b \quad (1)$$

176
 177 where τ_b represents the basal stress, N represents the effective pressure, and v_b is the magnitude
 178 of the basal velocity. For contemporary ice-free areas, a spatially varying basal friction coefficient
 179 is constructed to be proportional to bedrock elevation following Åkesson et al., 2018:

$$180 \quad k = 100 \times \frac{\min[\max(0, z_b + 800), z_b]}{\max(z_b)} \quad (2)$$

181
 182 where z_b is the height of the bedrock with respect to sea level. For these parametrizations, the
 183 friction coefficient is low within fjords and is larger over areas of high topographic relief. This
 184 basal friction coefficient is allowed to vary through time based upon changes in the simulated basal
 185 temperature following Cuzzone et al. (2019). As simulated basal ice temperatures decrease with
 186 respect to present day, the friction coefficient will increase, and therefore sliding will decrease.
 187
 188

189 The opposite occurs when simulated basal temperatures are warm relative to present day. Lastly,
 190 the ice rheology parameter B is temperature-dependent, following rate factors in Cuffey and
 191 Paterson (2010), and is initialized by solving for a present day thermal steady state and allowed to
 192 vary during transient simulations (Cuzzone et al., 2018; 2019).

193
 194
 195
 196
 197
 198

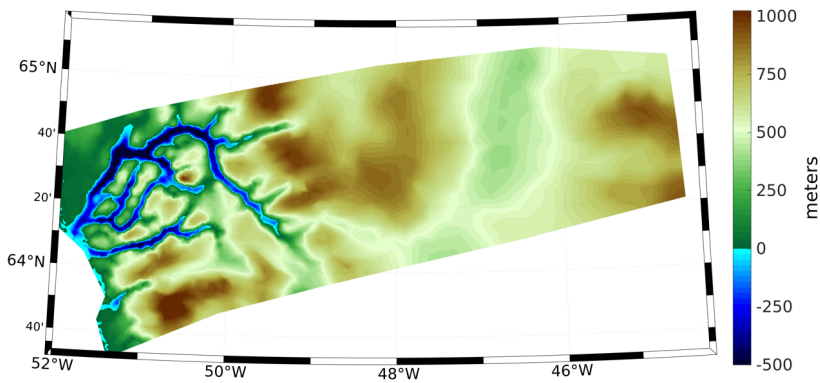


Figure 3. Bedrock topography for the model domain. Blue colors indicate areas that are below present-day sea level.

199
 200 **3.2 Ice Front Migration and Calving**

201 We use the level-set method to track the motion of the ice front (Bondzio et al., 2016). The velocity
 202 of the moving ice front is calculated as:

203
 204
 205
$$v_f = v - (c + M) n \tag{3}$$

206 where v_f is the ice velocity vector, v is the ice velocity vector at the ice front, c is the calving rate,
 207 M is the melting rate of the calving front, and n is the unit normal vector pointing horizontally
 208 outward from the calving front. For these simulations, we assume that the melting rate at the
 209 calving front is negligible compared to the calving rate.

210
 211 To simulate calving, we rely on the physically-based Von Mises stress calving (Morlighem et al.,
 212 2016), whereby the calving rate is related to tensile stresses within the ice:

213
 214
 215
$$c = \|v\| \frac{\sigma}{\sigma_{max}} \tag{4}$$

216
217
218
219
220
221
222
223
224
225
226
227
228
229
230
231
232
233
234
235
236
237
238
239
240
241
242
243

where σ is the von Mises tensile strength, $\|v\|$ is the magnitude of the horizontal ice velocity, and σ_{max} is the maximum stress threshold, which has separate values for grounded and floating ice. Under this formulation, the ice front will remain stable when $\sigma = \sigma_{max}$, will retreat when $\sigma > \sigma_{max}$, and will advance when $\sigma < \sigma_{max}$. Tensile strength measurements of ice show a range of possible σ_{max} , ranging between 150 kPa to 3100 kPa (Petrovic 2003). For this study we choose $\sigma_{max} = 600$ kPa for grounded ice and 200 kPa for floating ice, which is within the ranges used by recent studies across Greenland (Bondzio et al., 2016; Morlighem et al., 2016; Choi et al., 2020).

3.3 Climate and Surface Mass Balance Reconstruction

We rely on a novel gridded paleoclimate reanalysis product that reconstructs the necessary climate variables of temperature and precipitation needed to calculate the surface mass balance history through the Holocene (Badgeley et al., 2020). Temperature was derived from oxygen-isotope records from eight ice cores, and five ice core accumulation records were used to reconstruct precipitation. This reanalysis relies on a data assimilation framework that combines the information from ice core proxies with climate-model simulations of the last deglaciation (Liu et al., 2009; He et al., 2013) to create a spatially complete (e.g., GrIS wide) and temporally consistent reconstruction of past temperature and precipitation. This reconstruction agrees well with independent proxies and previously published paleoclimate reconstructions (Badgeley et al. (2020)). For new simulations presented here, we chose two end members of reconstructed precipitation and temperature from Badgeley et al. (2020). The high temperature reconstruction was chosen, which has a greater magnitude of **Early Holocene** warming, and the low temperature scenario, which has a more muted **Early Holocene** warming (Figure 4a). Additionally, we choose the high and low precipitation scenarios (Figure 4b), which differ in the magnitude and timing of peak Holocene precipitation. These reconstructions span a plausible range of temperature and precipitation scenarios as discussed in Badgeley et al. (2020).

Deleted: early Holocene
Deleted: early Holocene

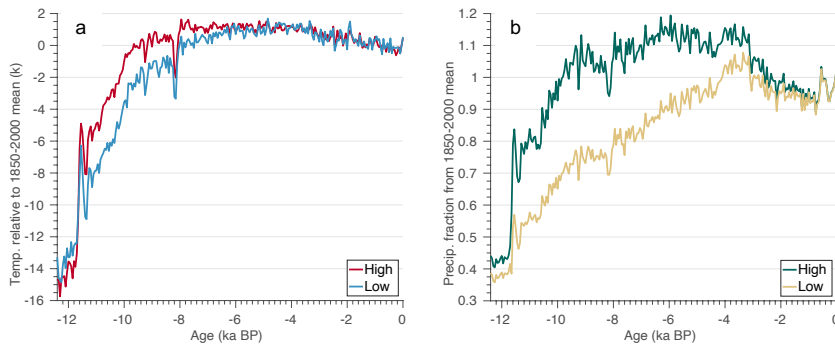


Figure 4. a) Area-averaged (over model domain) mean annual temperature anomaly (k) relative to the 1850-2000 mean for the High and Low temperature reconstructions from Badgeley et al. (2020). b) Area-averaged (over model domain) mean annual precipitation as a fraction from the 1850-2000 mean for the High and Low reconstructions from Badgeley et al. (2020).

246 The simulations discussed below use a combination of these forcings to address the possible role
247 of varying climatic conditions. Following prior work (Cuzzone et al., 2019; Briner et al., 2020),
248 we compute the surface mass balance over the Holocene using a positive degree day (PDD) method
249 (Tarasov and Peltier, 1999; Le Morzadec et al., 2015). For this scheme, snow melts first at 4.3
250 $\text{mm}^{-1}\text{C}^{-1}\text{day}^{-1}$ and the remaining positive degree days are used to melt bare ice at 8.3 $\text{mm}^{-1}\text{C}^{-1}\text{day}^{-1}$.
251 A lapse rate of 6 $^{\circ}\text{C}/\text{km}$ is used to adjust the temperature of the climate forcings to ice-surface
252 elevation, while an allowance for the formation of superimposed ice is permitted following
253 Janssens and Huybrechts (2000).

Deleted: $\text{mm}^{-1}\text{C}^{-1}\text{day}^{-1}$.

254 3.4 Experimental Setup

255 For the reanalysis discussed in section 3.3, temperature is expressed as anomalies from the AD
256 1850-2000 mean, and precipitation is expressed as a fraction of the AD 1850-2000 mean (Figure
257 4). Following Briner et al. (2020), we apply these anomalies onto the 1850-2000 monthly mean
258 climatology of temperature and precipitation from Box et al. (2013) to produce the necessary
259 Holocene temperature and precipitation forcings:

$$262 T_t = T_{(1850-2000)} + \Delta T_t \quad (5)$$

$$264 P_t = P_{(1850-2000)} \times \Delta P_t \quad (6)$$

265 where $T_{(1850-2000)}$ and $P_{(1850-2000)}$ are the monthly mean temperature and precipitation over AD
266 1850-2000 from Box et al. (2013) and ΔT_t and ΔP_t are the monthly anomalies from Badgeley et al.
267 (2020). We perform four transient model simulations using four combinations of possible climate
268 scenarios shown in Table 1. For each climate scenario, we run two simulations. First, simulations
269 are performed where the calving parameterization is turned on (denoted as ‘Calving On’). Second,
270 simulations are performed where the calving parameterization is turned off (denoted as ‘Calving
271 Off’). For these simulations, we apply a temporally constant melting rate under floating ice of 40
272 m/yr , which is consistent with contemporary melt rates derived near the grounding line of floating
273 ice shelves across the GrIS (Wilson et al., 2017). We also perform additional simulations discussed
274 further in section 4.4 to assess sensitivity to the calving maximum stress thresholds and ocean-
275 induced melt-rates.

276 We initialize our regional ice-sheet model using present-day ice-surface elevation from the
277 Greenland Ice Mapping Project digital elevation model (Howat et al., 2014). A constant climate
278 from 12,400 years ago is then applied for each experiment, allowing our model to reach
279 equilibrium in ice volume and basal temperature, which takes 20,000 years. Since our simulations
280 are regional in scale, we use boundary conditions of temperature, ice velocity, and thickness from
281 a recent ice sheet simulation of West-Southwest Greenland (Briner et al., 2020) and impose these
282 as Dirichlet boundary conditions at the southern, northern, and ice-divide boundaries. The eastern
283 boundary of our model domain extends outward to the present-day ice divide (Rignot and
284 Mouginit, 2012), with the northern and southern boundary of our model domain extending to
285 cover the KNS forefield. While the catchment for KNS may have changed during the Holocene
286 and thus may have impacted ice flux into our domain, those changes are not constrained.
287 Therefore, since we use consistent boundary conditions across our experiments, we consider that
288 our results are primarily influenced by the surface climate and oceanic boundary conditions applied

293 and not influenced by model domain extent. These boundary conditions are forced transiently
 294 throughout the Holocene simulations and use similar model setups and climate forcings as
 295 discussed here. Each model is then run transiently through time from 12,400 years ago to AD
 296 1850 using the climatologies discussed above, and then from 1850 to 2013 we use monthly
 297 temperature and precipitation fields from Box et al. (2013). We use an adaptive timestep, which
 298 varies between 0.02 and 0.1 years, depending on the Courant–Friedrichs–Lewy criterion (Courant
 299 et al., 1928). Discussed further in Section 5.3, we do not include glacial isostatic adjustment (GIA)
 300 in these simulations. Although GIA can influence the underlying bedrock topography and
 301 ultimately surface mass balance gradients and grounding line stability, changes during the
 302 Holocene across our domain are likely small (i.e. on the order of 100 meters; Caron et al., 2018),
 303 and therefore we expect this to have a minimal impact on our simulated ice histories.

Deleted:

	Temperature Scenario	Precipitation Scenario	Calving Parameterization
Experiment I	High	High	On
			Off
Experiment II	High	Low	On
			Off
Experiment III	Low	High	On
			Off
Experiment IV	Low	Low	On
			Off

314 **Table 1.** Description of model experiments. See Figure 4 for a display of the temperature and precipitation
 315 forcings scenarios.
 316

317
 318
 319 **4. Results**

320 We spin up each model as described above (section 3.4) without the ice calving parametrization
 321 turned on. Only when we begin the transient simulation through the Holocene do we turn on the
 322 ice calving parametrization for the ‘Calving On’ scenarios (Table 1). Our transient simulations
 323 begin 12,400 years ago with the ice margin residing along the present-day coastline for all
 324 experiments, which is approximately consistent with where geologic constraints place the ice
 325 margin at that time (Young et al., 2021 and references therein).
 326

Deleted: ,

327
 328 **4.1 Simulated Deglaciation**

329 First, we assess how our simulated deglaciation compares with geologic reconstructions of ice
 330 sheet change in the KNS region. Geological constraints outlined above reveal that ice retreated
 331 across the KNS forefield rapidly in the Early Holocene. While relatively little direct information
 332 exists detailing ice retreat within the fjords, the terrestrial portion of our domain (i.e., the inter-
 333 fjord bedrock landscape) became ice-free between ~11.2 ka and 9.5 ka as ice retreated from the
 334 modern coastline towards, and eventually surpassing, what is now the modern ice margin.
 335

Deleted: early Holocene

336 To compare against the geologic constraints, we determine when in time portions of our model
 337 domain become ice free (Figure 5). Since ice can readvance over areas that had been deglaciated
 338 during our simulations, we take the youngest age from which locations in our simulations became
 339

343 ice free. Our simulations illustrate clear differences in the timing of deglaciation across terrestrial
 344 surfaces above sea-level and within the fjords. For the high and low temperature scenarios,
 345 terrestrial surfaces deglacialate up to a few millennia earlier than the adjacent fjords. This difference
 346 in timing between the fjords and terrestrial surfaces is perhaps unsurprising given how fjord
 347 systems act as conduits draining the ice interior. This persistence of ice extent within the fjords
 348 despite elevated warming experienced during early to Middle Holocene illustrates the role of ice
 349 dynamics, which is explored further in section 4.3.

350
 351 For the high and low temperature scenarios, there is little difference between the age of
 352 deglaciation on terrestrial surfaces for simulations that allow (Figures 5a and 5b; Figures 6a and
 353 6b) and do not allow calving (Figures 5d and 5e; Figures 6d and 6e). In contrast, deglaciation of
 354 terrestrial surfaces occurs later in Holocene for the simulations using the high precipitation

Deleted: middle Holocene

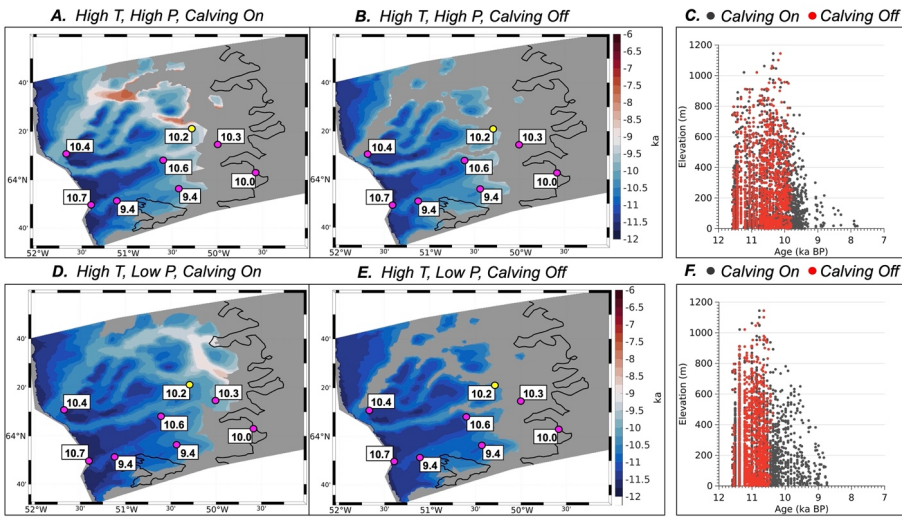


Figure 5. Map of simulated deglaciation ages for High temperature scenarios with A.) High precipitation, Calving On. B.) High precipitation, Calving Off. D.) Low precipitation, Calving On, and E.) Low precipitation – Calving off. Gray mask is the simulated ice extent at present day and the black line denotes the actual present day ice extent (Rignot and Mouginot, 2012). Magenta circles are the best estimate of the timing of deglaciation at that point based on ^{10}Be surface exposure ages in thousands of years ago and the yellow dot shows minimum limiting radiocarbon age (Young et al., 2021). Scatter plot of simulated deglaciation age (above sea level) versus bedrock elevation for C) High temperature, high precipitation, and F) High temperature, low precipitation. Red dots are from simulations without calving and black dots are for simulations with calving.

355 scenario than for those simulations using the low precipitation scenario. For simulations using the
 356 high temperature scenario, these differences are up to 500 years (Figure 5). For the low temperature
 357 scenarios, terrestrial surfaces deglacialate up to 1000 years later for simulations using the high
 358 precipitation forcing (Figure 6).

359

361 Lastly, it is important to note that simulations that allow calving have a more reduced ice extent
 362 (gray mask) at the end of each simulation, which may indicate that calving limits ice front
 363 readvance within the fjord.

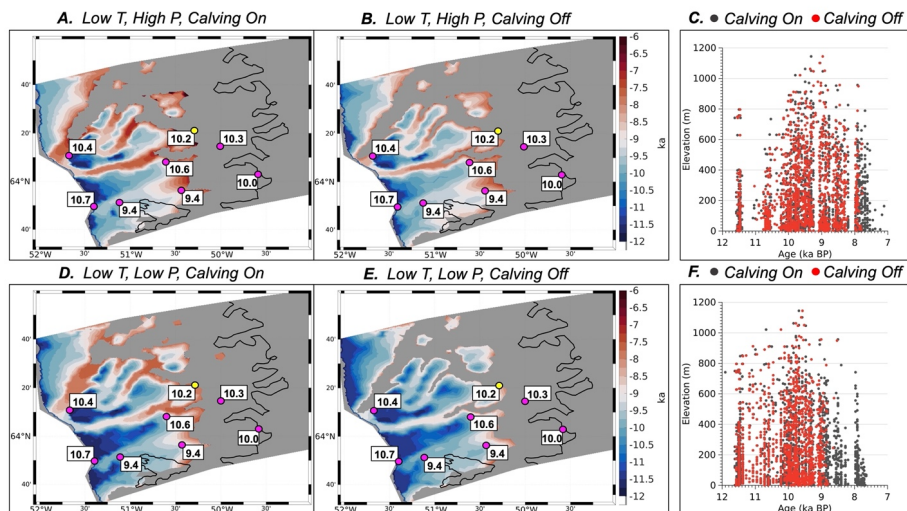


Figure 6. Map of simulated deglaciation ages for Low temperature scenarios with A.) High precipitation, Calving On. B.) High precipitation, Calving Off. D.) Low precipitation – Calving on, and E.) Low precipitation – Calving off. Gray mask is the simulated ice extent at present day and the black line denotes the actual present day ice extent (Rignot and Mouginot, 2012). Magenta circles are the best estimate of the timing of deglaciation at that point based on ^{10}Be surface exposure ages in thousands of years ago and the yellow dot shows a minimum limiting radiocarbon age that requires ice free conditions in the fjord at that time (Weidick et al., 2012; Young et al., 2021). Scatter plot of simulated deglaciation age (above sea level) versus bedrock elevation for C) Low temperature, high precipitation, and F) Low temperature, low precipitation. Red dots are from simulations without calving and black dots are for simulations with calving.

364
 365 The manner in which deglaciation occurs on terrestrial surfaces can be an important factor in
 366 determining the pace and magnitude of the ice margin response to warming. Geologic archives
 367 constraining ice retreat across the KNS forefield span an elevational range of 1300 m, yet, no
 368 elevational dependence on the age of deglaciation is evident (Larsen et al., 2014; Young et al.,
 369 2021). To compare our simulated deglaciation history as a function of elevation against the
 370 geologic data, we plot the simulated age of deglaciation against elevation, and restrict our
 371 datapoints to terrestrial surfaces above sea level (Figure 5c and 5f; Figure 6c and 6f). In general,
 372 our simulations agree with the geologic data indicating that there was no elevational dependence
 373 on the age of deglaciation; if there were any indication of an elevation dependence on the age of
 374 deglaciation, we would observe that high elevation sites would become ice free first, followed by
 375 low elevation sites. Instead, all of the plots show that deglaciation happens simultaneously at
 376 discrete time intervals across all elevation bands, indicating that ice surface lowering was rapid

~~Deleted: The larger sensitivity to the precipitation reconstruction on the timing of deglaciation for the lower temperature scenario versus the high temperature scenario is similar to the results of Briner et al. (2020): Across deglaciated regions where the surface mass balance dictates ice margin migration, increased precipitation modulates the temperature driven retreat in the early Holocene, particularly for simulations with colder climates (Briner et al., 2020; Downs et al., 2020). As discussed above, since calving does not appear to significantly influence terrestrial ice retreat across this region, SMB may be the primary driver of ice retreat across terrestrial surfaces within our model domain from which the majority of geologic constraints on past ice retreat are present.~~

~~Deleted: I~~

~~Deleted: , while calving does not seem to play a significant role in the retreat of ice across terrestrial surfaces,~~

Moved down [1]: This could indicate large scale ice margin retreat in response to rapid ice surface lowering, but certainly precludes scenarios where ice surface lowering occurred slowly exposing high elevation sites well before low elevation sites. T

399 and coincident with ice margin pullback. These elevation-time diagrams also highlight how the
400 higher precipitation scenarios have later mean deglaciation ages across terrestrial surfaces (Figure
401 5c and 6c) than corresponding simulations using the low precipitation scenario (Figure 5f and 6f).
402 We also note that for simulations where calving is turned off (red dots), ice retreat appears to stop
403 earlier than for those simulations with calving turned on (black dots). This occurs because the
404 simulations without calving experience a larger Late Holocene ice readvance than those
405 simulations where calving is turned on (black dots). As a consequence of this, model grid points
406 that would have otherwise deglaciated prior to the readvance are overrun with ice and therefore
407 are not marked as deglaciated in the simulation.

Deleted: late Holocene

409 Lastly, each of our experiments end with a simulated present-day ice extent that is beyond
410 (westward of) the actual present-day ice extent (Figure 5 and 6). Yet, the simulated ice-margin
411 position in the fjords is less extensive for all experiments where calving is permitted. Those
412 experiments that allow calving and used the high temperature scenario (Figure 5a and 5d) simulate
413 a present-day ice extent that is closer to the observed present-day margin when compared to
414 simulations using the low temperature forcing (Figure 6a and 6d).

415 4.2 Ice mass evolution and minimum ice extent

417 Broadly, scenarios that allow calving undergo greater ice mass loss than those simulations where
418 calving is not allowed (Figure 7; black lines). The differences in simulated ice mass also vary
419 depending on the climate scenarios used. For example, during Early Holocene warming (12 ka -
420 8 ka), simulations that allow calving and use the high temperature scenarios (Figure 7a, b)
421 experience ice mass loss, while simulations that do not allow calving experience a period of ice
422 mass stability (Figure 7a, b; dashed red line), which is more prolonged in the simulation using the
423 high precipitation scenario (Figure 7a).

Deleted: early Holocene

425 For the simulations using the low temperature scenario (Figure 7c, d), initial ice mass loss is
426 interrupted by brief increases in ice mass during the Early Holocene (between 11 ka-10 ka). This
427 increase in ice mass occurs for both scenarios with and without calving (Figure 7c, d; black and
428 dashed red line), although the simulations without calving experience larger increases in ice mass
429 during this period. Accordingly, the low temperature simulation with higher precipitation (Figure
430 7c) experiences larger ice mass gain than the simulation using the low precipitation scenario
431 (Figure 7d). During this interval, precipitation is approximately 20-30% more for the high
432 precipitation scenario during the Early Holocene than the low precipitation scenario. Much of this
433 mass gain is due to ice thickening over the interior of the model domain, where despite Early
434 Holocene warming, colder temperatures (at higher elevations on the ice sheet) support snowfall
435 (see section 4.3).

Deleted: early Holocene

Deleted: early Holocene

Deleted: early Holocene

437 Throughout the remainder of the Holocene, the evolution of ice mass for experiments using the
438 high temperature scenario (Figure 7a, b) differ from those simulations using the low temperature
439 scenario (Figure 7c, d). Simulations using the high temperature scenario (Figure 7a, b) reach a
440 minimum ice volume between 7.6-7.2 ka. For the simulation using the high precipitation scenario,
441 ice mass increases slightly following this minimum, and remains generally stable throughout the
442 remainder of the Holocene (Figure 7a), whereas the simulation using the low precipitation scenario
443 experiences large ice mass gain following this minimum, with steady growth occurring throughout
444

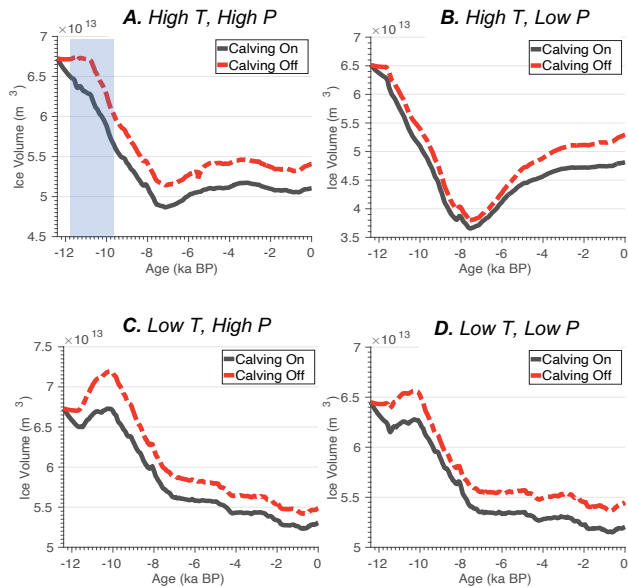


Figure 7. Holocene ice volume ($\times 10^{13} \text{ m}^3$) evolution for each model experiment. Refer to Table 1 for a summary of the climate forcings used in each experiment. Black lines denote those simulations with the calving parametrization turned on. Dashed red lines denote those simulations with the calving parametrization turned off. The vertical blue bar above marks a time period (12 ka – 10 ka) used for analysis presented in Figure 8 and 9.

450 the remainder of the simulation (Figure 7b). It is important to note, however, that for the high
 451 temperature scenarios, this ice mass gain is more muted for simulations that allow calving. In
 452 contrast, the simulations using the low temperature scenario (Figure 7c, d) lose the majority of ice
 453 mass by 8-7 ka, with ice mass loss either continuing through the Holocene (Figure 7c) or remaining
 454 relatively stable before reaching a minimum at 0.6-0.4 ka (Figure 7d).

455
 456 Regional relative sea-level records reveal that sea level fell below modern between 4-3 ka, before
 457 rising towards modern values (Long et al., 2011), interpreted to represent the re-loading of the
 458 Earth's crust as the GrIS readvanced during the Late Holocene following a mid-Holocene
 459 minimum. In addition, radiocarbon-dated lake sediments from southwestern Greenland suggest
 460 that this sector of the GrIS likely achieved its minimum extent after ca. 5 ka, and that eastwards
 461 retreat of the ice margin was likely minimal (Larsen et al., 2015; Young and Briner, 2015; Lesnek
 462 et al., 2020; Young et al., 2021). Although no direct geological constraints on the minimum GrIS
 463 ice extent during the Holocene exist, available constraints suggest that the magnitude of large-
 464 scale ice margin retreat inboard of the present-day extent as simulated by some ice sheet models
 465 in this sector (20-40 km; Tarasov and Peltier, 2002; Lecavalier et al., 2014) is likely too extreme.

Deleted: late Holocene

467 Relying on these geologic constraints, we can crudely assess the temporal and spatial patterns of
468 the simulated ice mass and minimum extent.

469
470 None of our simulations accurately capture the exact timing of the GrIS minimum in the KNS
471 region, but some simulations are likely better representations than others. Simulations using the
472 high temperature scenario (Figure 7a, b) achieve an ice mass minimum prior to 5 ka followed by
473 ice regrowth. The high temperature-low precipitation scenario depicts an extreme GrIS minimum
474 followed by significant regrowth. While of the overall pattern of a GrIS minimum followed by

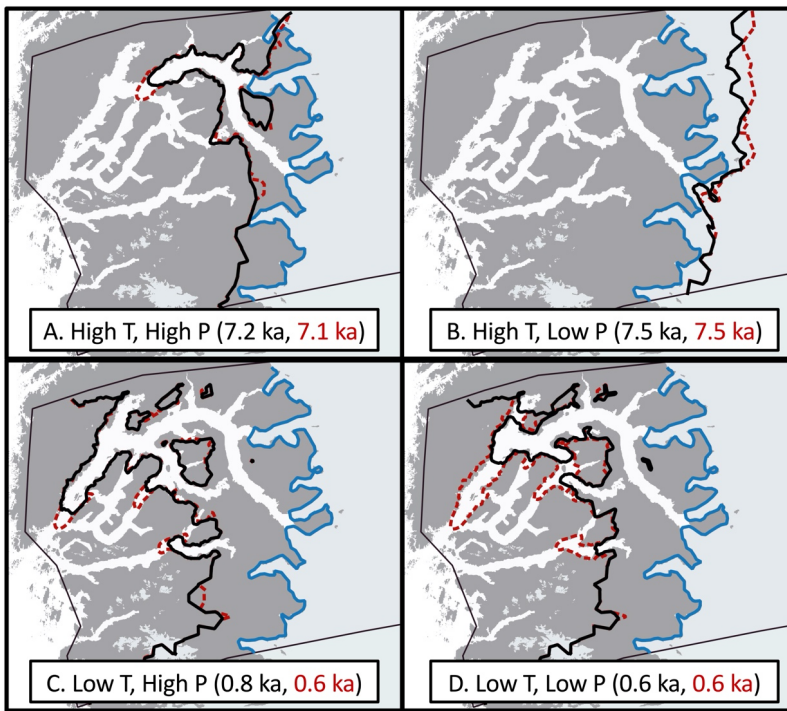


Figure 8. Age of minimum ice extent for each simulation (black text: simulations with calving, red text: simulations without calving). The black line denotes the minimum ice extent for simulations with calving. The dashed red line denotes the minimum ice extent for simulations without calving. The present-day ice extent is shown as the blue line.

475 regrowth is consistent with the geologic record, the magnitude of simulated change is likely
476 inconsistent with geological records, pointing to a rather modest GrIS minimum; although we do
477 acknowledge that minimal ice retreat as constrained by the geologic record does not necessarily
478 equate to muted mass loss. In contrast, the high temperature-high precipitation experiment depicts
479 an ice-mass minimum that is likely too early, but the magnitude of this minimum is less (Figure
480 7A). Moreover, ice regrowth following this minimum is restricted with only modest change

481 occurring over the last 6 kyr (Figure 7A). Although this simulated minimum is likely too early, a
482 simulated ice mass that undergoes minimal change over the last ~6 kyr is broadly consistent with
483 the geological record that depicts a minimum closer to ca. 4-3 ka, but where the GrIS margin likely
484 did not undergo significant change between ca. 7-3 ka (Young et al., 2021). Both low temperature
485 scenarios are inconsistent with the geological record as both show continued ice mass loss through
486 the Holocene. Although it is possible, but unlikely, that continued ice loss through the Holocene
487 could still be achieved if the ice margin retreated inland followed by a readvance toward its present
488 position, mass loss through the Holocene is inconsistent with relative sea-level records.

489
490 The minimum ice margin extent achieved in our simulations is shown in Figure 8. For the high
491 temperature scenarios (Figure 8a, b), the simulated minimum ice extent is either just outboard of
492 the present-day ice margin (Figure 8a; high precipitation) or inboard of the present-day ice margin
493 (Figure 8b; low precipitation). Because the geologic evidence supports that the Holocene ice
494 extent minimum was close to and perhaps slightly inboard of the present-day ice margin (Young
495 et al., 2021), both simulations are broadly consistent with the geological record. But, again, the
496 high temperature – high precipitation scenario depicts significant ice regrowth resulting in a
497 present-day ice margin significantly more extended than modern (Figure 5).

498 **4.3 Early Holocene Thinning**

501 Figures 9 and 10 show the simulated ice elevation changes for the time period between 12 ka to
502 10 ka for each experiment (highlighted in Figure 7a as the light blue vertical bar). During this time
503 period, widespread **Early Holocene** warming drove increased ice melt along the margin of the
504 model domain. This pervasive thinning along the margin is captured in all model experiments
505 (Figure 9 and 10), although the amplitude of ice thinning is greatest for the experiments using the
506 high temperature scenario (Figure 9). Across all experiments, inland thickening occurs, however,
507 the magnitude of interior thickening is not solely influenced by the **SMB**, but is also influenced by
508 calving. For our experiments that allow calving, interior thickening is reduced and ultimately
509 influences the trend and magnitude of changes in simulated ice volume; simulations that allow
510 calving either experience increased ice mass loss (Figure 7a, b) or more muted ice mass gain
511 between 12 ka and 10 ka (Figure 7c, d). Additionally, the spatial pattern of elevation changes
512 shows that marginal thinning propagates farther upstream and into the ice sheet interior for
513 simulations that allow ice calving. This relationship continues throughout the remainder of the
514 Holocene, as experiments with calving either result in more mass loss than simulations without
515 calving, or more muted ice mass gain (see Figure 7). These variations in simulated Holocene ice
516 mass and ice surface elevation change can be linked to the influence ice calving has on ice front
517 position and stability, and ultimately the rate at which ice can flux through the fjord system. During
518 the time period of 12 ka to 10 ka, ice velocity differences for simulations with and without calving
519 are in excess of 200 m/yr along many fjords within the KNS region (Figure 11). Calving at the
520 ice front leads to increases in ice velocity within outlets across the model domain, thereby
521 promoting increased mass flux and transport from the ice interior to the margin. Thus, even though
522 the large-scale ice margin migration across our model domain is relatively insensitive to calving,
523 the overall mass budget and surface profile of the ice is strongly influenced by calving.

Deleted: Early Holocene

Deleted: early Holocene

Deleted: SMB

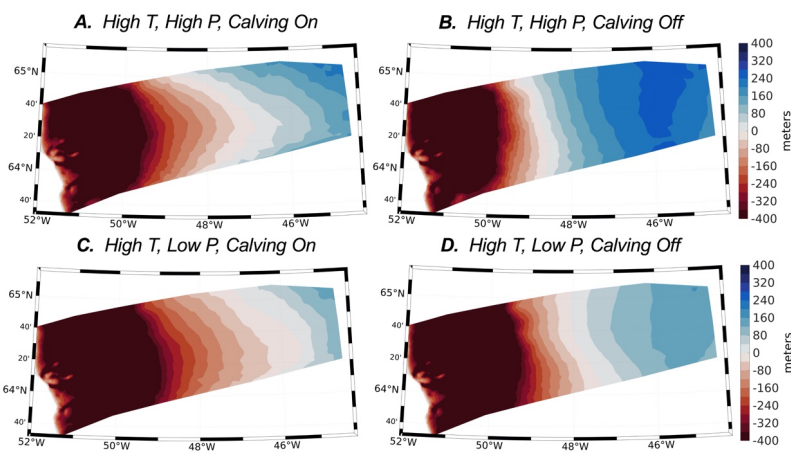


Figure 9. Simulated elevation changes (in meters) during period 12ka – 10ka shown for experiments using the high temperature forcing.

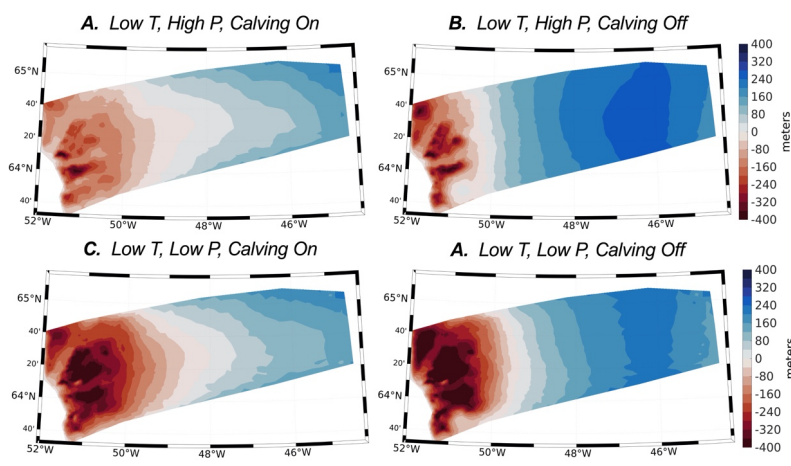


Figure 10. Simulated elevation changes during period 12ka-10ka shown for experiments using the low temperature forcing.

527
528
529
530
531

Reconstructions of Holocene ice thickness across the GrIS are limited, but ice-core records provide a long-term perspective of dynamic changes in GrIS elevation at locations at or near the ice divide (Vinther et al., 2009; Lecavalier et al., 2017). For example, some locations experienced more rapid thinning in response to Holocene warming (i.e. Camp Century, Dye 3) while other locations

532 experienced more muted ice elevation changes (i.e. GRIP, NGRIP). A feature of many of these
 533 records, however, is the presence of **Early Holocene** thickening, potentially triggered by increased
 534 snowfall at higher elevation sites as the climate warmed or by elevation-mass balance feedbacks
 535 driven by isostatic uplift (Vinther et al., 2009). Across all model experiments, our simulated timing
 536 of inland thickening coincides with thickening experienced at high elevation ice core locations
 537 (Vinther et al., 2009). The magnitude of **Early Holocene** thickening from ice core records (Vinther
 538 et al., 2009; 11.7 ka-10 ka) is on the order of 30 – 70 meters. Therefore, our simulations that allow
 539 calving display inland thickening (<120 m) over the time interval 12 ka – 10 ka that is more
 540 consistent with thickening estimated from ice cores than simulations with no calving (>200m).

Deleted: early Holocene

Deleted: early Holocene

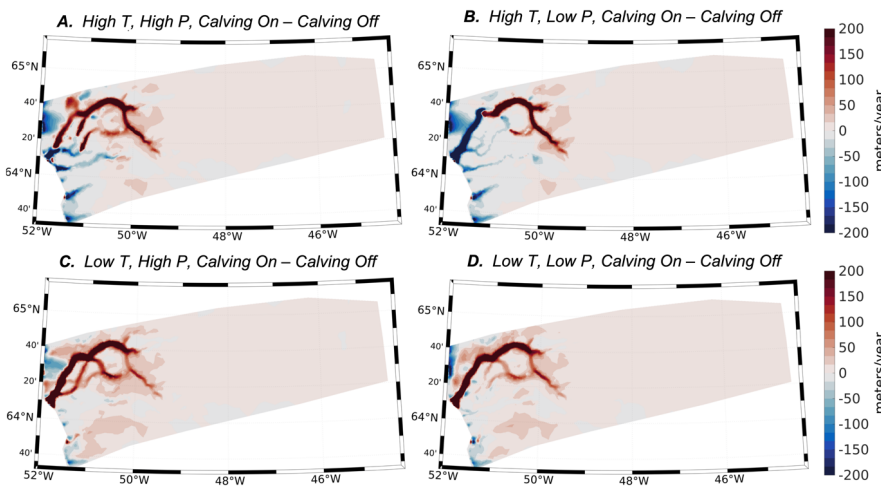


Figure 11. Simulated ice velocity differences between simulations with and without calving for each experiment over the time period 12 ka to 10 ka. Red colors denote an increase in ice velocity for simulations with calving relative to simulations without calving. Blue colors denote a decrease in ice velocity for simulations with calving relative to simulations without calving.

Deleted: Green

541
 542 **4.4 Sensitivity to marine forcing**
 543

544 Experiments on the tensile strength of ice show that stress thresholds can vary between 150 kPa
 545 and 3100 kPa (Petrovic, J. 2003), with modeling experiments on Jakobshavn glacier suggesting
 546 that the stress threshold for grounded ice can vary between 100 kPa to 4 MPa seasonally (Bondzio
 547 et al., 2017). Here, our grounded ice stress threshold is set to 600 kPa. Because our model setup
 548 incurs large computational expense, we did not perform a full uncertainty analysis on these
 549 parameterizations. Due to the nature of modeled variation in calibrated stress thresholds across
 550 Greenland (Choi et al., 2021), however, we ran a small set of experiments where we set the calving
 551 stress threshold on grounded ice to 1 MPa. We performed the transient simulations on the high
 552 and low temperature scenario cases using the high precipitation forcing (see Table 1).
 553 Additionally, we ran a set of experiments where the basal melt rate on floating ice was set to 120

Deleted: .

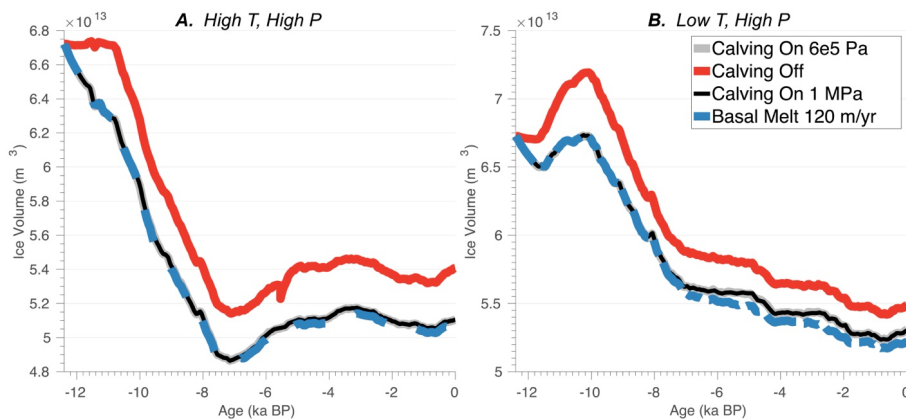


Figure 12. Sensitivity to the calving stress threshold for grounded ice and basal melt rates on floating ice. Red line: ice volume evolution for the simulations where the calving parameterization was turned off. Black line: ice volume evolution for the simulations where the calving stress threshold for grounded ice is 1 MPa. Gray line: ice volume evolution for the simulations where the calving stress threshold for grounded ice is 6 kPa. Dashed blue line: ice volume evolution for the simulations where the basal melt rate on floating ice was set to 120 m/yr (with calving stress threshold for grounded ice = 600 kPa).

557 m/yr. Figure 12 shows the simulated ice volumes for these experiments where the calving stress
 558 threshold of grounded ice and basal melt rate on floating ice were changed. These experiments
 559 reveal that adjusting the stress threshold from 600 kPa to 1 MPa has no effect on the evolution of
 560 the simulated ice volume. Accordingly, increasing the basal melt rate on floating ice has minimal
 561 effect on the simulated ice volume (Figure 12). Ice only begins to float in our experiments when
 562 the ice front retreats into the deeper fjord bathymetry within the KNS forefield (see Figure 3), and
 563 therefore submarine melting of floating ice seems to have limited influence on simulated ice mass
 564 changes.

565
 566 **5. Discussion**

567
 568 **5.1 Terrestrial vs. Marine ice retreat**

569
 570 Southwestern Greenland hosts a rich record of geologic constraints on past ice-sheet change
 571 (Lesnek et al., 2020). Whereas a series of well-defined moraines constrain Early Holocene ice
 572 retreat across portions of southwestern Greenland dominated by terrestrial ice-margin settings
 573 (Larsen et al., 2014; Lesnek et al., 2020; Young et al., 2020; Young et al., 2021), the Kapisigdlit
 574 moraine system (Figure 2: Early Holocene moraines) near the present-day ice margin is the only
 575 regionally traceable moraine within the marine-dominated KNS forefield. Instead, ice-margin
 576 retreat across the KNS forefield is constrained primarily by minimum limiting radiocarbon ages
 577 and ¹⁰Be surface exposure ages on deglaciated bedrock surfaces and glacial erratics (Larsen et al.,
 578 2014; Young et al., 2021). The lack of moraine systems between coast and ice is consistent with
 579 the relatively high rate of deglaciation estimated from the existing chronology. These
 580 chronological constraints detail widespread and rapid retreat of the ice margin across this domain

Deleted: early Holocene

Deleted: early Holocene

583 in the **Early Holocene**, with the ice margin retreating from the coastline around 12 ka to near the
584 present-day ice margin between 10-9.5 ka (Young et al., 2021). This relatively rapid retreat based
585 on geological observation is consistent with the lack of elevation-age relationship in our
586 simulations of ice margin change.

Deleted: early Holocene

587 While the rapid retreat of the terrestrial ice margin is well constrained, how ice retreated up the
588 fjords is less certain. Our simulations depict a pattern of ice retreat across the landscape that was
589 largely independent of ice retreat within fjords, which lagged by 0.5 – 2 ka. For our simulations,
590 scenarios using the same climate forcing show little difference (<1 ka) in the simulated age of ice
591 retreat on terrestrial ice margins regardless of whether calving is allowed (Figures 5 and 6). The
592 timing and rate of Holocene ice retreat across terrestrial portions of the KNS forefield, however,
593 is strongly dependent on the climate forcing used, and ultimately the **SMB**. The earliest ice retreat
594 occurs in simulations that use the high temperature scenario. Ice retreat occurs later in simulations
595 that use the low temperature scenario, which has a delay in the timing and magnitude of Holocene
596 warming (Figure 4). The pace and magnitude of ice retreat is shown to be modulated depending
597 on precipitation similar to the findings of Briner et al. (2020) and Downs et al. (2020), with delayed
598 and less rapid ice retreat in scenarios with higher precipitation (Figures 5a and 6a). These results
599 point to the strong influence that climate and, in particular, precipitation can have on modulating
600 the temperature driven response of Holocene deglaciation. Indeed, select proxy records suggest
601 that southwestern Greenland may have experienced a prolonged period of anomalously high
602 snowfall in the **Early Holocene**, perhaps driven by increased moisture flux from Baffin Bay and
603 the Labrador Sea as sea-ice extent declined (Thomas et al., 2016). Ice flow modeling across
604 southwestern Greenland has also revealed that elevated precipitation may have accompanied **Early**
605 **Holocene** warming (Downs et al., 2020). And recent evidence from a shallow ice core in western
606 Greenland reveal that significant variations in precipitation occurred in the last two thousand years
607 across the margins of the GrIS, whereas this variability is not present in ice core data at the interior
608 of the GrIS (Osman et al., 2021). Because current climate reconstructions employed in
609 paleoclimate ice flow modeling use either simple scaling approaches to reconstruct past climate or
610 rely on information from interior ice cores, large hydroclimate shifts that occur at the ice sheet
611 margin may not be captured (Badgeley et al., 2020). Continued progress in reconstructing past
612 climate will certainly improve our understanding of climatic controls on the long-term response of
613 the GrIS.

Deleted: SMB

Deleted: early Holocene

Deleted: early Holocene

616 In general, simulations using the high temperature scenario experience terrestrial ice retreat that
617 occurs during 11.5 ka to 9 ka, a time window consistent with the geological record of ice-margin
618 change in our domain (Larsen et al., 2014; Young et al., 2021). Simulations using the low
619 temperature scenario reveal terrestrial ice retreat also beginning ca. 11.5 ka, but deglaciation of
620 our model domain continues until ~7.5 ka. In comparison, geological constraints suggest that by
621 ~10.3-9 ka BP the ice margin in the immediate KNS region had already retreated back to, and
622 likely behind, what is the present-day ice margin (Young et al., 2021). Ice surface lowering is
623 captured in all of our simulations, which indicate that on terrestrial surfaces ice retreat was
624 synchronous across low and high elevations. Therefore, the simulated ice retreat could indicate
625 large scale ice margin retreat in response to rapid ice surface lowering, but certainly precludes
626 scenarios where ice surface lowering occurred slowly exposing high elevation sites well before
627 low elevation sites. While ice calving does not seem to significantly influence the rate and timing
628 of ice retreat across terrestrial portions of our domain, **Late Holocene** ice readvance within fjords

Moved (insertion) [1]

Deleted: is

Deleted:

Deleted: late Holocene

636 is more restricted in those simulations that use the calving parametrization. Accordingly, flowband
637 modeling of KNS over the period historical period of 1761 to 2012 suggests that marine ice-front
638 retreat was primarily influenced by atmospheric warming and runoff, which helped to trigger ice
639 front retreat via a crevasse-depth calving criterion, with submarine melting only playing a minor
640 role on historical retreat (Lea et al., 2014; Lea et al., 2014). These results do suggest though that
641 climate anomalies were the main driver of historical ice terminus advance and retreat across KNS
642 (Lea et al, 2014), with our results suggesting that the longer-term Holocene ice terminus position
643 was also primarily driven by atmospheric warming and not through oceanic melting.

644 5.2 Role of ice calving on mass transport

645 Mass transport from the ice sheet interior to the margin plays an important role in ice sheet mass
646 change and ultimately its contribution to sea-level rise. Contemporary satellite-derived
647 measurements show inland thickening at high elevations across portions of the GrIS in response
648 to increased snowfall despite pervasive thinning at lower elevations (Smith et al., 2020). Although
649 the response of marine terminating portions of the GrIS and how it translates to interior ice mass
650 loss can be spatially varying (Williams et al., 2021), thinning at the ice margin due to dynamic- or
651 ~~SMB~~-driven ice loss can elicit changes in driving stresses, which can propagate up glacier and into
652 the interior of the ice sheet (Price et al., 2008; Schlegel et al., 2013; Csatho et al., 2014; Felikson
653 et al., 2020; Williams et al., 2021).

Deleted: SMB

654 While there is no apparent influence of ice calving on the Holocene ice retreat across the KNS
655 forefield over terrestrial surfaces, our simulations show that ice calving has a significant influence
656 on the evolution of the total ice volume. Ultimately, ice calving leads to an acceleration of ice
657 flow within outlet glaciers that promotes local ice thinning first, followed by propagation of this
658 thinning into the interior of the ice sheet, consistent with contemporary observations (Csatho et
659 al., 2014; Williams et al., 2021). Initially, interior ice surface elevation increases in our
660 simulations, with simulations that allow calving being more consistent with ice-core derived
661 surface height records (Vinther et al., 2009). Surface lowering near the ice margin driven by a
662 more negative ~~SMB~~ in response to ~~Early Holocene~~ warming causes the ice surface slopes to
663 steepen in our domain, increasing driving stresses and mass transport. This helps drive interior ice
664 thinning, as shown by elevation changes in simulations that allow ice calving (Figures 9 and 10),
665 leading to increased ice flux at the margin through the ice streams (Figure 11). This increased
666 mass transport helps limit thinning within outlet glaciers, and where terrestrial locations of our
667 domain become ice free early in the Holocene, ice front retreat within the fjords lag (Figure 5 and
668 6).

Deleted: SMB

Deleted: early Holocene

669 Our results suggest that, while calving did not play a significant role in the observed Holocene ice
670 retreat across the KNS forefield, it played an important role on the overall ice mass change across
671 our model domain. These results highlight that the inclusion of physically based ice calving
672 parameterizations is an important step towards modeling the fidelity of simulated ice mass change
673 across paleoclimate timescales. However, the choice of which ice calving parameterization is best
674 suited to Greenland over such timescales is still not well constrained (Goelzer et al., 2017). It
675 remains important though, that models maintain high enough spatial resolution in order to capture
676 fjord environments, associated bathymetry, and ultimately ice calving and grounding line

684 migrations over paleoclimate timescales (Cuzzone et al., 2019) as the model resolution can impact
685 simulated ice discharge significantly (Rückamp et al., 2020; Ashwanden et al., 2019).

686

687 **5.3 Model limitations**

688

689 Fjord systems in Greenland are typically <5 km in width, making it necessary to implement high-
690 resolution meshes to resolve these features. Our model setup relies on a high-resolution mesh that
691 is able to capture the fjord geometry within the KNS forefield, making it possible to simulate
692 grounding line migration and calving. The calving parameterization used does ignore frontal
693 melting at the grounded ice front. Frontal melt at the base of a calving face has been shown to
694 induce undercutting of the ice front, and greatly increases calving rates (O’leary and
695 Christofferson, 2013). For the present day, many of southwestern Greenland’s marine terminating
696 glaciers are not strongly influenced by undercutting (Wood et al., 2021), but this may have been
697 different as ice retreated up fjord to its present-day location through the Holocene. *While proxy
698 records indicate changing sea surface temperatures during the Holocene proximal to our model
699 domain Axford et al. (2021), due to a lack of constraints on the long-term subsurface ocean thermal
700 forcing needed to implement undercutting in our simulations, we opted to disregard this. To
701 circumvent this shortcoming, we set our calving stress threshold on grounded ice to a number (600
702 kPa) that is on the lower end of measured tensile stresses of ice (Petrovic, 2003). Since there was
703 no discernable difference in our simulated ice mass change when a higher calving stress threshold
704 of grounded ice was used (1 MPa), we cautiously assume that implementation of undercutting
705 would have a negligible effect on the calving rates and overall Holocene mass change and ice
706 retreat across our domain. Future work will use a basal melt-rate parametrization (PICOP; Pelle
707 et al. 2019), employed in ISSM currently, to estimate oceanic melt rates from far field variations
708 in Holocene subsurface temperature and salinity in order to more robustly estimate the impact of
709 oceanic warming Holocene deglaciation across the GRS.*

Deleted: D

Deleted: long term

Deleted:

710

711 At the time of this work, ISSM is undergoing improvements and new implementation of solid earth
712 and sea-level feedbacks. While we did not include time dependent forcings (e.g. Caron et al.,
713 2018) that account for relative sea-level change as we have in prior research (Cuzzone et al., 2019;
714 Briner et al., 2020), future simulations using ISSM will explore the influence of coupled solid
715 Earth-ice feedbacks on ice retreat. Recent ice sheet modeling (Kajanto et al., 2020) showed that
716 the Holocene retreat of Jakobshavn Isbræ was insensitive to relative sea-level (RSL) variations, as
717 RSL changes were small in comparison to fjord depth. RSL changes during the Holocene across
718 this domain were relatively small (~60-100 meters at 12.4 ka and decreasing through the Holocene;
719 Caron et al., 2018) compared to fjord depths. Given that ice calving did not seem to largely
720 influence terrestrial ice retreat, we only expect that inclusion of Holocene RSL changes may have
721 influenced ice front retreat that migrated into deeper waters where floating extensions of the ice
722 front could occur. However, in our sensitivity tests, basal melting on floating ice plays a trivial
723 role in total ice volume changes (Figure 11) as most of the ice within fjords is grounded during the
724 Holocene retreat.

725

726 **6. Conclusions**

727

728 Understanding how climate, calving, and marine processes contribute to ice sheet change across
729 paleoclimate timescales is challenging. Models with lower resolution meshes are typically favored

733 to ensure computational needs are satisfied. This ultimately leads to poor representation of
734 bedrock topography (Cuzzone et al., 2019; Jones et al., 2021) and grounding line migration
735 (Seroussi et al., 2018) that control ice flow (i.e., fjords), making the assessment of how ice calving
736 influences large scale ice margin change difficult. Moreover, while ice core records provide
737 snapshots of a changing climate at the ice-sheet interior, there remain a relative lack of
738 paleoclimate records from the ice sheet margin of sufficient resolution that can be easily
739 incorporated into an ice sheet model's climate forcing.

740
741 Here, we presented results from a high-resolution 3D thermomechanical regional ice sheet model
742 that evaluated controls on the behavior of the southwestern GrIS during the Holocene in the
743 vicinity of the KNS forefield, an area with extensive geologic constraints on past ice margin
744 change. Experiments were driven by novel reconstructions of Holocene climate (Badgeley et al.,
745 2020) and included a physically based ice calving parametrization (Morlighem et al., 2016).

746
747 Our modeling results shed light on the well constrained observations of Holocene ice retreat across
748 the KNS forefield. ~~These~~ simulations agree well with observations that ice retreat on terrestrial
749 bedrock surfaces occurred rapidly between 11.5 ka to 9.5 ka in response to ~~Early Holocene~~
750 warming. ~~The~~ variations in the timing and magnitude of ice retreat on terrestrial bedrock surfaces
751 across this region are ~~found to be~~ insensitive to calving within the fjords that intersect this
752 landscape. ~~Instead, the terrestrial ice retreat is~~ more sensitive to the ~~SMB~~, with warmer climate
753 reconstructions providing the best fit between the modeled and observed ice retreat. Calving
754 ~~however does play a significant role in the~~ simulated Holocene ice volume change ~~across this~~
755 ~~domain~~. Acting as conduits for mass transport and ice flux, ice velocity within the fjords in the
756 KNS forefield increases when the ice front is allowed to calve. Calving helps promote further ice
757 mass transport from the interior of the domain to the ice front ~~which~~ helps to thicken ice within
758 the fjords, allowing the ice front to persist longer than adjacent terrestrial margins similar to the
759 ice response simulated for the Holocene retreat of Jakobshavn Isbræ (Kajanto et al., 2020). ~~These~~
760 ~~results suggest that paleo ice flow models that do not sufficiently resolve fjord geometry may not~~
761 ~~capture dynamic processes that are critical towards understanding long term ice mass change~~
762 ~~across the GrIS. Recent ice flow modelling has suggested that despite increased ice mass loss due~~
763 ~~to a more negative SMB, ice discharge from GrIS marine terminating glaciers will play a~~
764 ~~significant role in overall GrIS mass change well into the future (Choi et al., 2021). These results~~
765 ~~confirm that over paleoclimate timescales, while the SMB may dictate large scale ice margin~~
766 ~~migration as captured in geologic observations, ice discharge has the ability to greatly influence~~
767 ~~the rate and magnitude of ice mass change~~. However, as all simulations depict contemporary ice
768 extent that is too extensive, uncertainties in the reconstruction of past climate and model parametric
769 uncertainties ultimately contribute to misfits that are difficult to quantify given our
770 computationally expensive model setup. Future paleoclimate ice flow modelling with ISSM will
771 aim to take advantage of recent advances in statistical emulation (e.g., Edwards et al., 2021) to
772 better quantify the influence of model parametric uncertainty on simulated Holocene ice retreat.

773
774 Geologic archives serve an important role in our understanding of glacier and ice sheet response
775 to climate change. In turn, ice sheet modeling can help improve our understanding of the climatic
776 and ice dynamical factors that led to ice sheet changes preserved by the geologic record. Our
777 modeling results present an exploration of the factors that may have contributed to the observed
778 pattern of Holocene ice retreat across the KNS forefield, echoing that model–data comparisons

Deleted: Our

Deleted: early Holocene

Deleted: V

Deleted: , and is

Deleted: i

Deleted: SMB

Deleted: across this domain plays a significant role in the

Deleted: . This

Deleted:

788 between ice sheet models and geologic reconstructions can help improve our understanding of
789 long-term ice sheet sensitivity to climatic and dynamic forcing mechanisms.

790
791 **Data Availability**

792
793 The simulations performed for this paper made use of the open-source Ice Sheet System Model
794 (ISSM) version 4.19 and are publicly available at <https://issm.jpl.nasa.gov/> (Larour et al., 2012).

795
796 **Acknowledgements**

797
798 Funding for this study was provided by the National Science Foundation Grant ARC
799 no. 2105960 to JC and no. 1503959 to NEY. We thank the editor Caroline Clason, and James
800 [Lea and an anonymous reviewer for their constructive feedback regarding this work.](#)

801
802
803 **References**

- 804
805 Aschwanden, A., Bueler, E., Khroulev, C., and Blatter, H.: An enthalpy formulation for glaciers
806 and ice sheets, *J. Glaciol.*, 58, 441–457, <https://doi.org/10.3189/2012JoG11J088>, 2012.
807 Aschwanden, A., Fahnestock, M.A., Truffer, M., Brinkerhoff, D.J., Hock, R., Khroulev, C.,
808 Mottram, R., Khan, S.A. Contribution of the Greenland Ice Sheet to sea level over the
809 next millennium. *Science Advances*. 5. DOI: 10.1126/sciadv.aav9396. 2019.
810 Åkesson, H., Morlighem, M., Nisancioglu, K. H., Svendsen, J. J., and Mangerud, J.:
811 Atmosphere-driven ice sheet mass loss paced by topography: Insights from modelling the
812 south-western Scandinavian Ice Sheet, *Quaternary Sci. Rev.*, 195, 32–
813 47, <https://doi.org/10.1016/j.quascirev.2018.07.004>, 2018.
814 Axford, Y., de Vernal, A., Osterberg, E.C. Past Warmth and Its Impacts During the Holocene
815 Thermal Maximum in Greenland. *Annual Review of Earth and Planetary Sciences*.
816 49:279-307. <https://doi.org/10.1146/annurev-earth-081420-063858>.
817 Badgeley, J. A., Steig, E. J., Hakim, G. J., and Fudge, T. J.: Greenland temperature and
818 precipitation over the last 20 000 years using data assimilation, *Clim. Past*, 16, 1325–
819 1346, <https://doi.org/10.5194/cp-16-1325-2020>, 2020.
820 Blatter, H.: Velocity and stress-fields in grounded glaciers: A simple algorithm for including
821 deviatoric stress gradients, *J. Glaciol.*, 41, 333, 344
822 <https://doi.org/10.3189/S002214300001621X>, 1995.
823 Box, J. E.: Greenland ice sheet mass balance reconstruction. Part II: Surface mass balance
824 (1840–2010), *J. Clim.*, 26, 6974–6989, <https://doi.org/10.1175/JCLI-D-12-00518.1>, 2013.
825 Briner, J. P., McKay, N., Axford, Y., Bennike, O., Bradley, R. S., de Vernal, A., Fisher, D. A.,
826 Francus, P., Fréchet, B., Gajewski, K. J., Jennings, A. E., Kaufman, D. S., Miller, G.
827 H., Rouston, C., and Wagner, B.: Holocene climate change in Arctic Canada and
828 Greenland, *Quaternary Sci. Rev.*, 147, 340–364, 2016.
829 Briner, J. P., Cuzzone, J. K., Badgeley, J. A., Young, N. E., Steig, E. J., Morlighem, M.,
830 Schlegel, N.-J., Hakim, G., Schaefer, J. Johnson, J. V., Lesnek, A. L., Thomas, E. K.,
831 Allan, E., Bennike, O., Cluett, A. A., Csatho, B., de Vernal, A., Downs, J., Larour, E.,
832 and Nowicki, S.: Rate of mass loss from the Greenland Ice Sheet will exceed Holocene
833 values this century, *Nature*, 6, 70–74, <https://doi.org/10.1038/s41586-020-2742-6>, 2020.

Formatted: Font: Times, 12 pt, Font color: Text 1

Formatted: Font color: Text 1, Not Highlight

Formatted: Font color: Text 1

Formatted: Font: Times, 12 pt, Font color: Text 1

Formatted: Font color: Text 1, Not Highlight

Formatted: Font: Times, 12 pt, Font color: Text 1

Formatted: Font: Times, Font color: Text 1

Formatted: Indent: Left: 0"

Deleted: <https://doi.org/10.1146/annurev-earth-081420-063858>

- 836 Bondzio, J. H., Seroussi, H., Morlighem, M., Kleiner, T., Rückamp, M., Humbert, A., and
837 Larour, E. Y.: Modelling calving front dynamics using a level-set method: application to
838 Jakobshavn Isbræ, West Greenland, *The Cryosphere*, 10, 497–510,
839 <https://doi.org/10.5194/tc-10-497-2016>, 2016.
- 840 Bondzio, J., Morlighem, M., Seroussi, H., Kleiner, T., Rückamp, M., Mouginot, J., Moon, T.,
841 Larour, E., Humbert, A. The mechanisms behind Jakobshavn Isbrae’s acceleration and
842 mass loss: a 3-D thermomechanical model study. *Geophys. Res. Lett.*, 44 (12) pp. 6252-
843 6260, 10.1002/2017GL073309, 2017
- 844 Caron, L., Ivins, E. R., Larour, E., Adhikari, S., Nilsson, J., and Blewitt, G.: GIA model statistics
845 for GRACE hydrology, cryosphere and ocean science, *Geophys. Res. Lett.*, 45, 2203–
846 2212, <https://doi.org/10.1002/2017GL076644>, 2018.
- 847 Choi, Y., Morlighem, M., Rignot, E. *et al.* Ice dynamics will remain a primary driver of
848 Greenland ice sheet mass loss over the next century. *Commun Earth Environ* 2, 26.
849 <https://doi.org/10.1038/s43247-021-00092-z>, 2021
- 850 Courant, R., Friedrichs, K. & Lewy, H. Über die partiellen Differenzgleichungen der
851 mathematischen Physik. *Math. Ann.* 100, 32–74, 1928
- 852 Cuffey, K. M. and Paterson, W. S. B.: The physics of glaciers, 4th edn., Butterworth-Heinemann,
853 Oxford, 2010.
- 854 Cuzzone, J., Morlighem, M., Larour, E., Schlegel, N., Seroussi, H.: Implementation of
855 higher-order vertical finite elements in ISSM v4.13 for improved ice sheet flow modeling
856 over paleoclimate timescales, *Geosci. Model Dev.*, 11, 1683–
857 1694, <https://doi.org/10.5194/gmd-11-1683-2018>, 2018.
- 858 Cuzzone, J. K., Schlegel, N.-J., Morlighem, M., Larour, E., Briner, J. P., Seroussi, H., Caron,
859 L.: The impact of model resolution on the simulated Holocene retreat of the southwestern
860 Greenland ice sheet using the Ice Sheet System Model (ISSM), *The Cryosphere*, 13, 879–
861 893, <https://doi.org/10.5194/tc-13-879-2019>.
- 862 Csatho, B.M., Schenk, A.F., van der Veen, C., Babonis, G., Duncan, K., Rezvanbehbahani, S.,
863 van den Broecke, M.R., Simonsen, S.B., Nagarajan, S., van Angelen, J.H. Laser
864 altimetry reveals complex pattern of Greenland ice sheet dynamics. *Proceedings of the
865 National Academy of Sciences* 111, 18478–18483, 2014
- 866 Downs, J., Johnson, J., Briner, J., Young, N., Lesnek, A., and Cuzzone, J.: Western Greenland
867 ice sheet retreat history reveals elevated precipitation during the Holocene thermal
868 maximum, *The Cryosphere*, 14, 1121–1137, <https://doi.org/10.5194/tc-14-1121-2020>,
869 2020.
- 870 Edwards, T. L., Nowicki, S., Marzeion, B., Hock, R., Goelzer, H., Seroussi, H., Jourdain,
871 N. C., Slater, D. A., Turner, F. E., Smith, C. J., McKenna, C. M., Simon, E., Abe-Ouchi,
872 A., Gregory, J. M., Larour, E., Lipscomb, W. H., Payne, A. J., Shepherd, A., Agosta, C.,
873 Alexander, P., Albrecht, T., Anderson, B., Asay-Davis, X., Aschwanden, A., Barthel, A.,
874 Bliss, A., Calov, R., Chambers, C., Champollion, N., Choi, Y., Cullather, R., Cuzzone, J.,
875 Dumas, C., Felikson, D., Fettweis, X., Fujita, K., Galton-Fenzi, B. K., Gladstone, R.,
876 Gollede, N. R., Greve, R., Hattermann, T., Hoffman, M. J., Humbert, A., Huss, M.,
877 Huybrechts, P., Immerzeel, W., Kleiner, T., Kraaijenbrink, P., Le clec’h, S., Lee, V.,
878 Leguy, G. R., Little, C. M., Lowry, D. P., Malles, J.-H., Martin, D. F., Maussion, F.,
879 Morlighem, M., O’Neill, J. F., Nias, I., Pattyn, F., Pelle, T., Price, S. F., Quiquet, A.,
880 Radić, V., Reese, R., Rounce, D. R., Rückamp, M., Sakai, A., Shafer, C., Schlegel, N.-J.,
881 Shannon, S., Smith, R. S., Straneo, F., Sun, S., Tarasov, L., Trusel, L. D., Van Breedam,

Deleted: and

Deleted: and

884 J., van de Wal, R., van den Broeke, M., Winkelmann, R., Zekollari, H., Zhao, C., Zhang,
885 T., and Zwinger, T.: Projected land ice contributions to twenty-first-century sea level rise,
886 *Nature*, 593, 74–82, <https://doi.org/10.1038/s41586-021-03302-y>, 2021.

887 Felikson, D., Catania, G., Bartholomäus, T.C., Morlighem, M. and Noël, B. Steep glacier bed
888 knickpoints mitigate inland thinning in Greenland. *Geophysical Research Letters*.
889 doi: 10.1029/2020GL090112, 2020

890 He, F., Shakun, J. D., Clark, P. U., Carlson, A. E., Liu, Z., Otto-Bliesner, B. L., and Kutzbach,
891 J. E.: Northern Hemisphere forcing of Southern Hemisphere climate during the last
892 deglaciation, *Nature*, 494, 81–85, 10.1038/nature11822, 2013

893 Howat, I. M., Negrete, A., and Smith, B. E.: The Greenland Ice Mapping Project (GIMP) land
894 classification and surface elevation datasets, *The Cryosphere*, 8, 1509–
895 1518, <https://doi.org/10.5194/tc-8-1509-2014>, 2014.

896 IMBIE Team. Mass balance of the Greenland Ice Sheet from 1992 to 2018. *Nature*, 579
897 (7798) pp. 233–239. 10.1038/s41586-019-1855-2, 2019

898 Enderlin, E. M., Howat, I. M., Jeong, S., Noh, M. J., van Angelen, J. H., & van den Broeke, M.
899 R. An improved mass budget for the Greenland ice sheet. *Geophysical Research Letters*,
900 41, 866–872. <https://doi.org/10.1002/2013GL059010>. 2014

901 Vizcaino, M. Ice sheets as interactive components of Earth System Models: Progress and
902 challenges. *Wiley Interdisciplinary Reviews: Climate Change*, 5(4), 557–568.
903 <https://doi.org/10.1002/wcc.285>, 2014

904 Goelzer, H., Robinson, A., Seroussi, H. *et al.* Recent Progress in Greenland Ice Sheet
905 Modelling. *Curr Clim Change Rep* 3, 291–302 [https://doi.org/10.1007/s40641-017-0073-](https://doi.org/10.1007/s40641-017-0073-y)
906 y, 2017

907 Goelzer, H., Nowicki, S., Payne, A., Larour, E., Seroussi, H., Lipscomb, W. H., Gregory, J.,
908 Abe-Ouchi, A., Shepherd, A., Simon, E., Agosta, C., Alexander, P., Aschwanden, A.,
909 Barthel, A., Calov, R., Chambers, C., Choi, Y., Cuzzone, J., Dumas, C., Edwards, T.,
910 Felikson, D., Fettweis, X., Gollledge, N. R., Greve, R., Humbert, A., Huybrechts, P., Le
911 clec'h, S., Lee, V., Leguy, G., Little, C., Lowry, D. P., Morlighem, M., Nias, I., Quiquet,
912 A., Rückamp, M., Schlegel, N.-J., Slater, D., Smith, R., Straneo, F., Tarasov, L., van de
913 Wal, R., and van den Broeke, M.: The future sea-level contribution of the Greenland ice
914 sheet: a multi-model ensemble study of ISMIP6, *The Cryosphere*,
915 <https://doi.org/10.5194/tc-2019-319>, 2020.

916 Fettweis, X., Hanna, E., Gallée, H., Huybrechts, P., & Erpicum, M. Estimation of the
917 Greenland ice sheet surface mass balance for the 20th and 21st centuries. *The*
918 *Cryosphere*, 2(2), 117–129. <https://doi.org/10.5194/tc-2-117-2008>, 2008

919 Janssens, I., and P. Huybrechts. The treatment of meltwater retention in mass-balance
920 parameterizations of the Greenland ice sheet, *Ann. Glaciol.*, 31, 133– 140.
921 10.3189/172756400781819941, 2000

922 Jones, R.S., Whitmore, R.J., Mackintosh, A.N., Norton, K.P, Eaves, S.R, Stutz, J., Christl, M.
923 Regional-scale abrupt Mid-Holocene ice sheet thinning in the western Ross Sea,
924 Antarctica. *Geology*, 49 (3): 278–282. doi: <https://doi.org/10.1130/G48347.1>, 2020

925 Kajanto, K., Seroussi, H., de Fleurian, B., Nisancioglu, K.H. Present day Jakobshavn
926 Isbræ (West Greenland) close to the Holocene minimum extent. *Quaternary Science*
927 *Reviews*, 24, <https://doi.org/10.1016/j.quascirev.2020.106492>, 2020

928 Larour, E., Seroussi, H., Morlighem, M., and Rignot, E.: Continental scale, high order, high

Deleted: ¶

Formatted: Indent: Left: 0"

Deleted: ¶

Formatted: Indent: Left: 0"

931 spatial resolution, ice sheet modeling using the Ice Sheet System Model (ISSM), J.
 932 Geophys. Res.-Earth, 117, F01022, <https://doi.org/10.1029/2011JF002140>, 2012.

933 Larsen, N. K., Funder, S., Kjær, K. H., Kjeldsen, K. K., Knudsen, M. F., and Linge, H.: Rapid
 934 **Early Holocene** ice retreat in West Greenland, *Quaternary Sci. Rev.*, 92, 310–
 935 323, <https://doi.org/10.1016/j.quascirev.2013.05.027>, 2014.

936 Lecavalier, B. S., Milne, G. A., Simpson, M. J. R., Wake, L., Huybrechts, P., Tarasov, L.,
 937 Kjeldsen, K. K., Funder, S., Long, A. J., Woodroffe, S., Dyke, A. S., and Larsen, N. K.:
 938 A model of Greenland ice sheet deglaciation constrained by observations of relative sea
 939 level and ice extent, *Quaternary Sci. Rev.*, 102, 54–
 940 84, <https://doi.org/10.1016/j.quascirev.2014.07.018>, 2014.

941 Lea, J. M., Mair, D. W. F., Nick, F. M., Rea, B. R., van As, D., Morlighem, M., Nienow, P. W.,
 942 and Weidick, A.: Fluctuations of a Greenlandic tidewater glacier driven by changes in
 943 atmospheric forcing: observations and modelling of Kangiata Nunaata Sermia, 1859–
 944 present, *The Cryosphere*, 8, 2031–2045, <https://doi.org/10.5194/tc-8-2031-2014>, 2014.

945 Lea, J. M., Mair, D. W. F., Nick, F. M., Rea, B. R., Weidick, A., Kjær, K. H., Morlighem, M.,
 946 van As, D., and Schofield, J. E.: Terminus-driven retreat of a major southwest Greenland
 947 tidewater glacier during the early 19th century: insights from glacier reconstructions and
 948 numerical modelling, *J. Glaciol.*, 60, 333–344, <https://doi.org/10.3189/2014JoG13J163>,
 949 2014.

950 Lecavalier, B. S., Fisher, D. A., Milne, G. A., Vinther, B. M., Tarasov, L., Huybrechts, P.,
 951 Lacelle, D., Main, B., Zheng, J., Bourgeois, J., and Dyke, A. S.: High Arctic Holocene
 952 temperature record from the Agassiz ice cap and Greenland ice sheet evolution, *P. Natl.*
 953 *Acad. Sci. USA*, 23, 5952–5957, <https://doi.org/10.1073/pnas.1616287114>, 2017.

954 Le Morzadec, K., Tarasov, L., Morlighem, M., and Seroussi, H. 2015. A new sub-grid surface
 955 mass balance and flux model for continental-scale ice sheet modelling: testing and last
 956 glacial cycle, *Geosci. Model Dev.*, 8, 3199–3213, <https://doi.org/10.5194/gmd-8-3199-2015>.

957

958 Lenaerts, J. T. M., Medley, B., van den Broeke, Michiel R., & Wouters, B. Observing and
 959 modeling Ice-Sheet surface mass balance. *Reviews of Geophysics*, 57(2), 376-420.
 960 doi:10.1029/2018RG000622, 2019.

961 Lesnek, A. J., Briner, J. P., Young, N. E., and Cuzzone, J. K.: Maximum southwest Greenland
 962 Ice Sheet recession in the **Early Holocene**, *Geophys. Res. Lett.*, 47,
 963 e2019GL083164, <https://doi.org/10.1029/2019GL083164>, 2020.

964 Liu, Z., Otto-Bliesner, B., He, F., Brady, E., Tomas, R., Clark, P., Carlson, A., Lynch-Stieglitz,
 965 J., Curry, W., Brook, E., Erickson, D., Jacob, R., Kutzbach, J., and Cheng, J.: Transient
 966 simulation of last deglaciation with a new mechanism for Bølling-Allerød warming,
 967 *Science*, 325, 310–314, <https://doi.org/10.1126/science.1171041>, 2009

968 Morlighem, M., Rignot, E., Seroussi, H., Larour, E., Ben Dhia, H., and Aubry, D.: Spatial
 969 patterns of basal drag inferred using control methods from a full-Stokes and simpler
 970 models for Pine Island Glacier, West Antarctica, *Geophys. Res. Lett.*, 37,
 971 L14502, <https://doi.org/10.1029/2010GL043853>, 2010.

972 Morlighem, M., Bondzio, J., Seroussi, H., Rignot, E., Larour, E., Humbert, A.,
 973 Rebuffi, S., Modeling of Store Gletscher's calving dynamics, West Greenland, in
 974 response to ocean thermal forcing, *Geophys. Res. Lett.*, 43,
 975 doi:10.1002/20116GL067695, 2016

Deleted: early Holocene

Deleted: early Holocene

978 Morlighem, M., Williams, C. N., Rignot, E., An, L., Arndt, J. E., Bamber, J. L., Catania, G.,
979 Chauché, N., Dowdeswell, J. A., Dorschel, B., Fenty, I., Hogan, K., Howat, I., Hubbard,
980 A., Jakobsson, M., Jordan, T. M., Kjeldsen, K. K., Millan, R., Mayer, L., Mouginot, J.,
981 Noël, B. P. Y., Ó Cofaigh, C., Palmer, S., Rysgaard, S., Seroussi, H., Siegert, M. J.,
982 Slabon, P., Straneo, F., van den Broeke, M. R., Weinrebe, W., Wood, M., and Zinglensen,
983 K. B.: BedMachine v3: Complete bed topography and ocean bathymetry mapping of
984 Greenland from multi-beam echo sounding combined with mass conservation, *Geophys.*
985 *Res. Lett.*, 44, 11051–11061, <https://doi.org/10.1002/2017GL074954>, 2017
986 O'Leary, M. and Christoffersen, P.: Calving on tidewater glaciers amplified by submarine frontal
987 melting, *The Cryosphere*, 7, 119–128, <https://doi.org/10.5194/tc-7-119-2013>, 2013.
988 Osman, M.B., Smith, B.E., Trusel, L.D., Das, S.B., McConnell, J.R., Chellman, N., Arienzo, M.,
989 Sodemann, H. Abrupt Common Era hydroclimate shifts drive west Greenland ice cap
990 change. *Nat. Geosci.* 14, 756–761 (2021). <https://doi.org/10.1038/s41561-021-00818-w>
991 Pattyn, F.: A new three-dimensional higher-order thermomechanical ice sheet model: Basic
992 sensitivity, ice stream development, and ice flow across subglacial lakes, *J. Geophys.*
993 *Res.*, 108, 2382, <https://doi.org/10.1029/2002JB002329>, 2003.
994 **Pelle, T., Morlighem, M., and Bondzio, J. H.: Brief communication: PICOP, a new ocean melt**
995 **parameterization under ice shelves combining PICO and a plume model, *The Cryosphere*,
996 **13, 1043–1049, <https://doi.org/10.5194/tc-13-1043-2019>, 2019.**
997 Petrovic, J. J. Review Mechanical properties of ice and snow. *J. Mater. Sci.* 38, 1–6, 2003
998 Price, SF, Payne, AJ, Catania, GA and Neumann, TA. Seasonal acceleration of inland ice via
999 longitudinal coupling to marginal ice. *Journal of Glaciology* 54(185), 213–219, 2008
1000 Rignot, E. and Mouginot, J.: Ice flow in Greenland for the international polar year 2008–2009,
1001 *Geophys. Res. Lett.*, 39, L11501, <https://doi.org/10.1029/2012GL051634>, 2012.
1002 Rückamp, M., Greve, R., Humbert, A. Comparative simulations of the evolution of the
1003 Greenland ice sheet under simplified Paris Agreement scenarios with the models
1004 SICOPOLIS and ISSM. *Polar Science*. 21, 14–25.
1005 <https://doi.org/10.1016/j.polar.2018.12.003>. 2019.
1006 Schlegel, N.J., Larour, E., Seroussi, H., Morlighem, M., Box, J.E., Decadal-scale sensitivity of
1007 northeast Greenland ice flow to errors in surface mass balance using ISSM *J. Geophys.*
1008 *Res. - Earth Surface*, 118, doi: 10.1002/jgrf.20062. 2013.
1009 Seroussi, H. and Morlighem, M.: Representation of basal melting at the grounding line in ice
1010 flow models, *The Cryosphere*, 12, 3085–3096, <https://doi.org/10.5194/tc-12-3085-2018>.
1011 2018
1012 Shapiro, N. M. and Ritzwoller M. H.: Inferring surface heat flux distribution guided by a global
1013 seismic model: particular application to Antarctica, *Earth Planet. Sc. Lett.*, 223, 213–
1014 224, <https://doi.org/10.1016/j.epsl.2004.04.011>, 2004.
1015 Smith B, Fricker HA, Gardner AS, Medley B, Nilsson J, Paolo FS, Holschuh N, Adusumilli S,
1016 Brunt K, Csatho B, Harbeck K, Markus T, Neumann T, Siegfried MR, Zwally HJ.
1017 Pervasive ice sheet mass loss reflects competing ocean and atmosphere processes.
1018 *Science*. 368(6496):1239-1242. doi: 10.1126/science.aaz5845, 2020
1019 Smith-Johnsen, S., Schlegel, N.-J., de Fleurian, B., & Nisancioglu, K. H. Sensitivity of the
1020 Northeast Greenland Ice Stream to geothermal heat. *Journal of Geophysical Research:*
1021 *Earth Surface*, 125, e2019JF005252. <https://doi.org/10.1029/2019JF005252>, 2020
1022 Thomas, E. K., Briner, J. P., Ryan-Henry, J. J., and Huang, Y.: A major increase in winter
1023 snowfall during the **Middle Holocene** on western Greenland caused by reduced sea ice in**

- Formatted: Font: 11 pt
- Formatted: Font: Times, 11 pt
- Formatted: Font: 11 pt
- Formatted: Font: 11 pt
- Formatted: Font: 11 pt
- Formatted: Font: Times
- Formatted: Font: Times
- Formatted: Font: 11 pt, Bold, Font color: Custom Color(RGB(70,70,70))
- Formatted: Justified, Indent: Left: 0", First line: 0", Pattern: Clear (White)

Deleted: middle Holocene

1025 Baffin Bay and the Labrador Sea, *Geophys. Res. Lett.*, 43, 5302–
1026 5308, <https://doi.org/10.1002/2016GL068513>, 2016

1027 Vinther, B., Buchardt, S., Clausen, H. *et al.* Holocene thinning of the Greenland ice
1028 sheet. *Nature* 461, 385–388, <https://doi.org/10.1038/nature08355>, 2009

1029 Weidick, A., Bennike, O., Citterio, M., and Nøgaard-Pedersen, N.: Neoglacial and historical
1030 glacier changes around Kangarsuneq fjord in southern West Greenland, *Geol. Surv. Den.*
1031 *Greenla.*, 27, 1–68. <https://doi.org/10.34194/geusb.v27.4694>, 2012.

1032 Williams, J. J., Gourmelen, N., Nienow, P. Complex multi-decadal ice dynamical change inland
1033 of marine-terminating glaciers on the Greenland Ice Sheet. *Journal of Glaciology*. 1–14.
1034 <https://doi.org/10.1017/jog.2021.31>, 2021.

1035 [Wilson, N., Straneo, F., and Heimbach, P.: Satellite-derived submarine melt rates and mass](#)
1036 [balance \(2011–2015\) for Greenland's largest remaining ice tongues. *The Cryosphere*, 11,](#)
1037 [2773–2782. <https://doi.org/10.5194/tc-11-2773-2017>.](#)

1038 Wood, M., Rignot, E., Fenty, I., An, L., Bjørk, A., van den Broeke, M., Cai, C., Kane, E.,
1039 Menemenlis, D., Millan, R., Morlighem, M., Mouginot, J., Noël, B., Scheuchl, B.,
1040 Velicogna, I., Willis, J. K., & Zhang, H. Ocean forcing drives glacier retreat in
1041 Greenland. *Science Advances*, 7(1), <https://doi.org/10.1126/sciadv.aba7282>, 2021

1042 Young, N. E. and Briner, J. P.: Holocene evolution of the western Greenland Ice Sheet:
1043 Assessing geophysical ice-sheet models with geological reconstructions of ice-margin
1044 change, *Quaternary Sci. Rev.*, 114, 1–17, <https://doi.org/10.1016/j.quascirev.2015.01.018>,
1045 2015.

1046 Young, N.E., Briner, J.P., Miller, G.H., Lesnek, A.J., Crump, S.E., Thomas, E.K., Pendleton,
1047 S.L., Cuzzone, J., Lamp, J., Zimmerman, S., Caffee, M., Schaefer, J.M., 2020.
1048 Deglaciation of the Greenland and Laurentide ice sheets interrupted by glacier advance
1049 during abrupt coolings. *Quat. Sc. Rev.* 229, 106091.

1050 Young, N. E., Lesnek, A. J., Cuzzone, J. K., Briner, J. P., Badgeley, J. A., Balter-Kennedy, A.,
1051 Graham, B. L., Cluett, A., Lamp, J. L., Schwartz, R., Tuna, T., Bard, E., Caffee, M. W.,
1052 Zimmerman, S. R. H., and Schaefer, J. M.: In situ cosmogenic ^{10}Be – ^{14}C – ^{26}Al
1053 measurements from recently deglaciated bedrock as a new tool to decipher changes in
1054 Greenland Ice Sheet size, *Clim. Past*, 17, 419–450, [https://doi.org/10.5194/cp-17-419-](https://doi.org/10.5194/cp-17-419-2021)
1055 2021, 2021.

Formatted: Font: Times

Formatted: Font: Times

Formatted: Font: Times, 12 pt

Formatted: Indent: Hanging: 0.5"

Formatted: Font color: Auto